

High resolution spatially extended 1D laser scattering diagnostics using volume Bragg grating notch filters

Cite as: Rev. Sci. Instrum. **94**, 023003 (2023); <https://doi.org/10.1063/5.0121436>

Submitted: 17 August 2022 • Accepted: 18 January 2023 • Published Online: 08 February 2023

 J. Bak,  J. L. Suazo Betancourt,  A. Rekhy, et al.



View Online



Export Citation



CrossMark

ARTICLES YOU MAY BE INTERESTED IN

Neutron imaging of inertial confinement fusion implosions



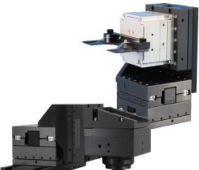
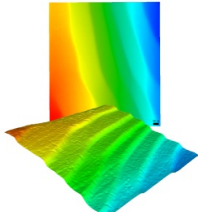
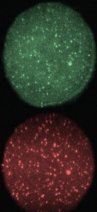
Review of Scientific Instruments **94**, 021101 (2023); <https://doi.org/10.1063/5.0124074>

Machine learning for detection of 3D features using sparse x-ray tomographic reconstruction

Review of Scientific Instruments **94**, 023504 (2023); <https://doi.org/10.1063/5.0101681>

Design and performance of a double-solenoid magnetic bottle photoelectron spectrometer for attosecond metrology

Review of Scientific Instruments **94**, 023303 (2023); <https://doi.org/10.1063/5.0105623>

 MAD CITY LABS INC. www.madcitylabs.com	<p>Nanopositioning Systems</p> 	<p>Modular Motion Control</p> 	<p>AFM and NSOM Instruments</p> 	<p>Single Molecule Microscopes</p> 
---	--	--	---	--

High resolution spatially extended 1D laser scattering diagnostics using volume Bragg grating notch filters

Cite as: Rev. Sci. Instrum. 94, 023003 (2023); doi: 10.1063/5.0121436

Submitted: 17 August 2022 • Accepted: 18 January 2023 •

Published Online: 8 February 2023



J. Bak,^{1,a)} J. L. Suazo Betancourt,² A. Rekhy,¹ A. Abbasszadehrad,¹ R. B. Miles,¹ C. M. Limbach,¹ and M. L. R. Walker²

AFFILIATIONS

¹Department of Aerospace Engineering, Texas A&M University, 400 Bizzell St., College Station, Texas 77843, USA

²Daniel Guggenheim School of Aerospace Engineering, Georgia Institute of Technology, North Ave. NW, Atlanta, Georgia 30332, USA

^{a)}Author to whom correspondence should be addressed: junhwib@tamu.edu

ABSTRACT

Laser light scattering systems with volume Bragg grating (VBG) filters, which act as spectral/angular filters, have often been used as a point measurement technique, with spatial resolution as low as a few hundred μm , defined by the beam waist. In this work, we demonstrate how VBG filters can be leveraged for spatially resolved measurements with several μm resolution over a few millimeters along the beam propagation axis. The rejection ring, as determined by the angular acceptance criteria of the filter, is derived analytically, and the use of the ring for 1D laser line rejection is explained. For the example cases presented, i.e., for a focused probe beam waist with a diameter of $\sim 150 \mu\text{m}$, the rejection ring can provide resolution up to several millimeter length along the beam propagation axis for a 1D measurement, which is also tunable. Additionally, methods to further extend the measurable region are proposed and demonstrated, using a collimation lens with a different focal length or using multiple VBG filters. The latter case can minimize the scattering signal loss, without the tradeoff of the solid angle. Such use of multiple VBGs is to extend the measurable region along the beam axis, which differs from the commonly known application of multiple filters, to improve the suppression of elastic interferences. 1D rotational Raman and Thomson scattering measurements are carried out on pulsed and DC discharges to verify this method. The system features compactness, simple implementation, high throughput, and flexibility, to accommodate various experimental conditions.

Published under an exclusive license by AIP Publishing. <https://doi.org/10.1063/5.0121436>

I. INTRODUCTION

Laser light scattering is an important diagnostic tool. It allows remote access to physically harsh test articles in high-pressure/high-temperature environments, where measurements by a physical probe are practically limited. With proper consideration on laser-induced perturbation,^{1,2} it can achieve non-perturbative measurements. Accurate measurement of the relevant state quantities of the scatterers, such as temperature and density, allow for the validation of physical simulation models, ultimately leading to a better understanding of physics and better design of specific applications. This is due to the minimal assumptions required in order to employ these laser light scattering techniques, which may not even require local thermal equilibrium.

Scattering configurations are typically off-axis of the laser beam propagation axis, with the practical maximum signal being collected perpendicular to the beam polarization direction. The laser-focused beam waist is strongly localized, providing high spatial resolution that is set by the beam waist and another limiting aperture. This configuration produces a localized measurement in contrast with path-integrated techniques such as optical emission spectroscopy and microwave interferometry, which require tomographic methods to spatially resolve the measurements. Along the laser beam, the spatial resolution is determined by the optics and a detection camera's resolution in the case of a free-space optical detection system. This can be several tens of μm . Meanwhile, the maximum resolution perpendicular to the beam is determined by the beam waist, which is typically about 100–200 μm .

Different scatterers in the detection volume, such as monatomic and polyatomic neutral gas particles, ions, and electrons, will scatter differently. Knowledge of the scatterers and detection parameters allow for direct measurement of some of their key state properties. Rayleigh scattering is elastic light scattering by the induced dipole moment from bound electrons and can be used to measure the gas temperature, velocity, and density.³ Raman scattering, an inelastic scattering process associated with the transition in a molecule's rotational or vibrational state, provides molecular number densities and the rotational/vibrational temperatures. Thomson scattering from free electrons allows measuring electron temperature, density, drift velocity,^{4,5} and the electron energy distribution function—⁶fundamental properties that define the composition of plasma.⁷

The intensity of the elastically scattered light (Rayleigh scattering and stray light) is often several orders higher than that of Raman or Thomson scattering. In weakly ionized plasmas, where the neutral density is much greater than the plasma density, Rayleigh scattering dominates, whereas in fully ionized plasmas, Thomson scattering is dominant; however, in both cases, stray light from laser reflections often overwhelms the signals and needs to be suppressed. Differential scattering cross-sections $d\sigma/d\Omega$ of different particles for the right-angle-scattering⁸ in $10^{-32} \text{ m}^2\text{sr}^{-1}$ are 3.9 for Rayleigh (N_2), 0.054 for rotational Raman ($\text{N}_2 J-J' = 6-8$), and 794 for Thomson (e^-). It is also noteworthy that the intensity of the stray light can also be significantly close to the laser line because of reflections and other factors that allow this light to make it through the detection system if left unaddressed. The Thomson signal in many plasma applications, such as low-temperature, weakly ionized plasma, becomes difficult to detect because the neutral density is several orders of magnitude greater than the electron density. Thus, to detect Raman and Thomson scattering signals, the light near the laser line (Rayleigh scattering/stray light) should be effectively removed to prevent saturation of the detector. Such laser line rejection can be performed with multiple techniques, such as a triple grating spectrograph,⁸⁻¹⁶ a vapor cell,¹⁷⁻¹⁹ a glass/interference filter,²⁰ a physical mask,^{21,22} and a volume Bragg grating (VBG) filter.²³⁻²⁹

Past data analysis from laser scattering experiments using the VBG filter were effectively limited to point measurements,^{23-26,29,30} which may have been a significant limitation of the method. Recent works by Wu *et al.*²⁷ present one-dimensional (1D) measurements of Thomson scattering of a nanosecond, repetitively pulsed discharge, using a VBG filter, showing the possible extension of spatial measurement of light scattering. However, no detailed explanation of the use is given.

In this paper, we elaborate on the details of how to realize 1D measurement with VBG filters based on the first principles of VBG filter rejection characteristics. Several useful equations to characterize the rejection region are provided. The equations help determine design parameters, such as a measurable length and a resolution, for the design stage of such a system. Additionally, we propose a method to further extend the measurement region using multiple VBGs. It should be noted that this proposed method differs from the commonly known application of multiple VBGs to improve the rejection capability. The extended measurement volume along the laser propagation axis by VBG filters is expected to be greatly advantageous, by maintaining the desired spatial resolution perpendicular to the beam

propagation axis for applications that require high throughput light scattering diagnostics.

II. PRINCIPLE OF VOLUME BRAGG GRATING FILTERS

A. General background

The VBG is a diffractive grating that rejects light at certain wavelengths and given angular conditions by refractive index modulation in the volume of a photosensitive material. Depending on the design of the diffraction angle/orientation/modulation, VBGs can be of several types, such as transmitting Bragg gratings (TBGs), reflecting Bragg gratings (RBGs), or chirped Bragg gratings (CBGs). Among these VBGs, RBGs exhibit two characteristic features—a narrow band spectral filter and an angular filter. Configured as a narrow-band notch filter, RBGs have spectral bandwidths as narrow as 5 cm^{-1} .²⁴ A filter allows the selective reflection of light at a specifically designed wavelength incidence at the Bragg condition, thus performing a dual function—as an angular filter and as a spectral filter. A detailed theoretical model of volume gratings can be found elsewhere.³¹⁻³³

The use of the reflecting VBG as a notch filter for light scattering diagnostics provides several advantages. First, the optical systems required for signal collection are significantly simplified; in the simplest case, the optical system consists of two lenses, a VBG filter, a single grating spectrometer, and an intensified detector. This naturally leads to a significant improvement in the system's total efficiency through the use of minimal optics. Additional throughput is gained through the transmittance of the filter outside of the spectral rejection region, with transmittance of the unfiltered wavelengths being up to 95%. Additionally, the method provides excellent flexibility in the system design. Depending on the necessity of a specific experiment, simply adding an additional filter can improve the total laser line rejection and spatial extension of the measurement region, while maintaining throughputs that are an order of magnitude higher than those of multi-stage spectrometers.

Commercially available reflecting volume Bragg gratings used as notch filters show spectral bandwidths as narrow as 5 cm^{-1} .²⁴ A typical transmittance curve of an OD4 filter designed for 532 nm (BNF-532; OptiGrate) as a function of incident angle to the filter surface is shown in Fig. 1. The curve data are read from a specification sheet provided by OptiGrate. Approximately within 0.1° of the designed input angle 6° , the filter provides 10^{-4} attenuation. This angular spectrum characteristic is a key element to realize a 1D measurement with BNFs for light scattering diagnostics.

B. Evaluation of a rejection ring and manipulation of the rejection ring position

The transmittance curve as a function of the incident angle to the filter surface, in Fig. 1, shows that 10^{-4} transmission is attainable within $6 \pm 0.05^\circ$ and 10^{-3} transmission is attainable within $6 \pm 0.09^\circ$. This indicates that only a certain *spatial range* of light from the object plane can be rejected by the filter if the incident angle of the approximately collimated light falls within the ranges given above. We define the rejecting angle θ_r , and the OD4 and OD3 range as $\delta\theta_{\text{OD4}}$ and $\delta\theta_{\text{OD3}}$, respectively. $\theta_r = 6^\circ$, $\delta\theta_{\text{OD4}} = 0.05^\circ$, and $\delta\theta_{\text{OD3}} = 0.09^\circ$ are used as example values for a filter in the following evaluation.

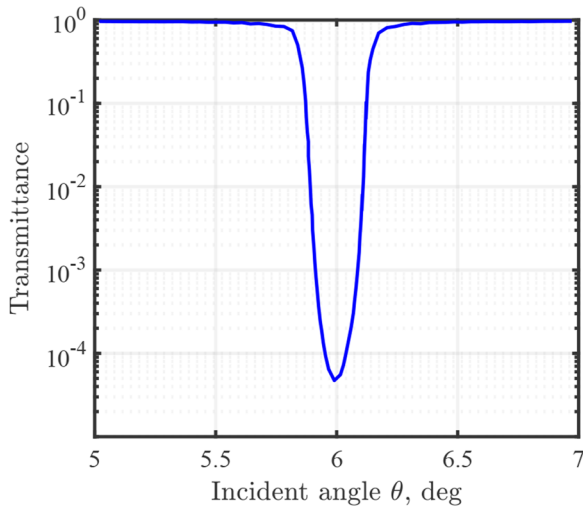


FIG. 1. Typical angular spectrum for an OD4, reflecting volume Bragg grating filter (data from OptiGrade).

Let us consider an optical arrangement of a collimating lens and a VBG, as shown in Fig. 2, where

- \vec{c} is a position vector of the center of the collimation lens, and $\vec{c} = [0, 0, f]^T$ in the x - y - z coordinate, where f is a focal length of the collimation lens.
- \vec{p} is a position vector of a point p on the object plane.
- \vec{s} is a vector from the point p to the center of a collimation lens, $\vec{s} \equiv \vec{c} - \vec{p}$.
- \vec{e}_s is a unit vector of \vec{s} , $\vec{e}_s \equiv \vec{s}/|\vec{s}|$.
- \vec{n} is a unit normal vector of the Bragg notch filter plane. The initial orientation $\vec{n}_i = [0, 0, 1]^T$.

For a scattering source p on the object plane as a point source, the light scattered by the source is collimated by the lens, assuming that the lens is one focal length away from the object plane. Note that the direction of the collimated rays is determined by a ray directly pointing at the center of the collimation lens from the source p . This collimated ray vector is denoted as \vec{s} . Then, the angle θ between \vec{s}

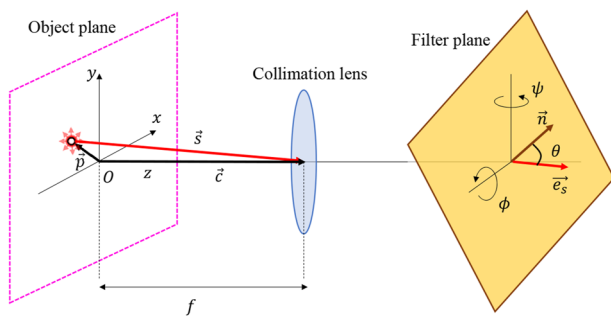


FIG. 2. Schematic of an optical arrangement among an object plane, a collimation lens, and a filter plane.

and \vec{n} becomes the incident angle of the ray to the filter, which can be obtained by

$$\theta = \cos^{-1}(\vec{e}_s \cdot \vec{n}). \quad (1)$$

Thus, by calculating θ for each location on the object plane and taking into account the transmittance from Fig. 1, the spatial distribution of a rejected region can be identified, which eventually turns out to be a ring shape. We term this rejected area as the *rejection ring*, the justification for which will be shown below. It is noteworthy that the described spatial rejection region analysis can be fundamentally applicable to any type of angular/spectral filters, such as interference filters or holographic spectral filters. Using the angular spectra given in Fig. 1, a rejection ring (center) diameter D_r can be estimated as

$$D_r = 2f \tan \theta_r, \quad (2)$$

and the thickness of the OD4 ring $t_{r,OD4}$ is

$$t_{r,OD4} = f(\tan(\theta_r + \delta\theta_{OD4}) - \tan(\theta_r - \delta\theta_{OD4})), \quad (3)$$

and the thickness of the OD3 ring $t_{r,OD3}$ is

$$t_{r,OD3} = f(\tan(\theta_r + \delta\theta_{OD3}) - \tan(\theta_r - \delta\theta_{OD3})). \quad (4)$$

Note that different VBGs having different angular rejection properties will have different rejection incident angles and OD4/OD3 ranges, which can be obtained from their specifications. The reason for evaluating the two OD rings is because one can choose either ring for a diagnostic system design, depending on the attenuation requirement of the test condition in a trade-off between the attenuation and the spatial rejection size, as well as other factors such as cost and lead time.

Figure 3 shows a sample calculated incident angle distribution (a) and a light intensity map (b). For this calculation, $f = 100$ mm is used, and an initial intensity, $I = 10^4$, is given for every location on the object plane. The position having the incident angle $\theta = 6^\circ$ is indicated as a black solid line in (a), and accordingly, the rejected region appears in the shape of a ring in (b). For the intensity map, the angular transmittance curve in Fig. 1 is used. $D_r \approx 21$ mm, $t_{r,OD4} \approx 177$ μ m, and $t_{r,OD3} \approx 318$ μ m are obtained.

Now, we consider angle tuning of the filter plane with two degrees of freedom—a rotation with respect to the x axis (pitch control) and a rotation with respect to the y axis (yaw control), using Euler angles. Note that the rotation along z axis has no effect due to the axisymmetric relation, which is enforced through collinearity of the optics (placing the optics along the same optical axis). We can determine the angle of any vector from one plane (or frame of reference) to any other plane, by relating it through a matrix transformation, using rotation matrices.

Defining a rotation matrix for each of the angles above, one with respect x axis (pitch) with an angle ϕ as

$$R_x(\phi) \equiv \begin{bmatrix} 1 & 0 & 0 \\ 0 & \cos \phi & -\sin \phi \\ 0 & \sin \phi & \cos \phi \end{bmatrix}, \quad (5)$$

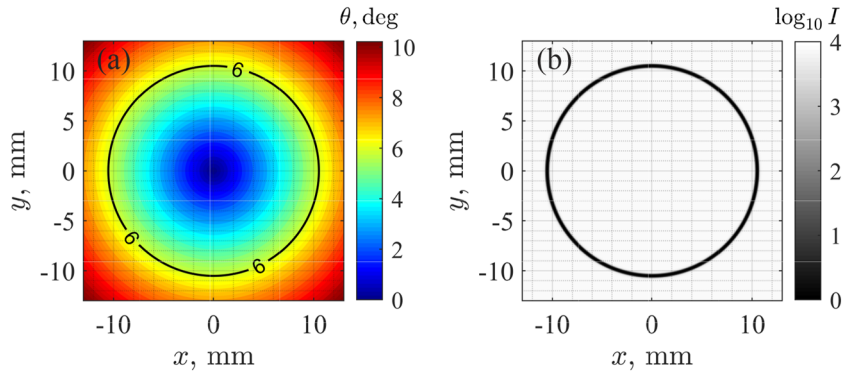


FIG. 3. (a) A map of the incident angle θ to the filter surface, depending on the position of the scattering source on the object plane. (b) A map of light intensity I , where the initial intensity $I = 10^4$ was over the whole object plane. The attenuation by the filter on a specific ring-shape region is observable.

and a rotation matrix of the angle with respect to y axis with a yaw angle ψ as

$$R_y(\psi) \equiv \begin{bmatrix} \cos \psi & 0 & -\sin \psi \\ 0 & 1 & 0 \\ -\sin \psi & 0 & \cos \psi \end{bmatrix}, \quad (6)$$

the normal vector of the filter \vec{n} is obtained as

$$\vec{n} = R_x(\phi)R_y(\psi)\vec{n}_i. \quad (7)$$

Then, a final angle θ that rays from the point p form with respect to the VBG can be obtained by Eq. (1).

Influence of the pitch/yaw angle adjustment is shown in Fig. 4, with (a) being a map of incident angle θ for a pitch angle $\phi = 6^\circ$, (b) a map of light intensity I for $\phi = 6^\circ$, (c) a map of incident angle θ for a yaw angle $\psi = 6^\circ$, and (d) a map of light intensity I for $\psi = 6^\circ$. Note that a ϕ control moves the rejection ring up and down along the y axis, and a ψ control moves the image's rejection ring left and right along the x axis.

For rejection, we are concerned with the relative size and location of the rejection ring on the image of the laser beam region, imaged at our detector plane. This is because, without any rejection, the detector saturates, due to redistribution of the strong laser line light from Rayleigh scattering, as well as reflections through the collection system. Therefore, the laser line light must be adequately blocked in the field of view of our detector in order to be

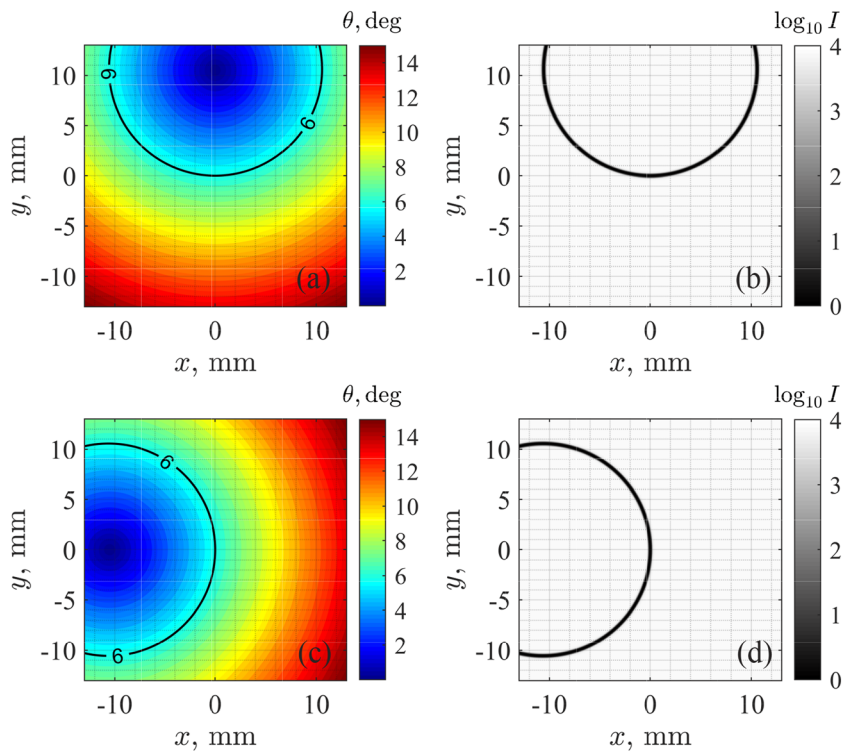


FIG. 4. (a) A map of incident angle θ for a pitch angle $\phi = 6^\circ$, (b) a map of light intensity I for $\phi = 6^\circ$, (c) θ for a yaw angle $\psi = 6^\circ$ and (d) I for $\psi = 6^\circ$.

able to collect the relatively weak, rotational Raman and Thomson scattering lights. For a given VBG, collimating/objective lens and focusing/imaging lens, the size of the rejection ring on the image of the laser beam at the imaging plane, as well as its position on the laser beam image, can be directly controlled, by controlling the pitch and yaw angles, assuming good collimation through the collimating lens. This can be further controlled with a second VBG.

C. Customization of VBG parameters

It should be noted that the analysis here was made based on the default designed parameters of a specific filter given in Fig. 1. Compared to the conventional surface-relief gratings, the VBG has greater parameter space of peak efficiency and dispersion, so, customization of the grating parameters can be easily attained.³⁴ A detailed model of the reflecting VBG³³ based on Kogelnik's coupled wave theory³⁵ provides several practical formulas, with grating parameters such as diffraction efficiency η_0 , spectral selectivity at a half width at first zero (HWFZ) $\delta\lambda^{\text{HWFZ}}$, angular selectivity $\delta\theta_m^{\text{HWFZ}}$, incident Bragg angle θ_m^* , and grating thickness t_0 . For instance, $\delta\lambda^{\text{HWFZ}}$ and $\delta\theta_m^{\text{HWFZ}}$ are given as follows:³³

$$\delta\lambda^{\text{HWFZ}} = \frac{\lambda_0^2 \left[\left(\operatorname{atanh} \sqrt{\eta_0} \right)^2 + \pi^2 \right]^{1/2}}{2\pi n_{\text{av}} t_0 |\cos \theta_m^*|}, \quad (8)$$

$$\delta\theta_m^{\text{HWFZ}} = \begin{cases} \left(\tan^2 \theta_m^* + \frac{2\delta\lambda^{\text{HWFZ}}}{\lambda_0} \right)^{1/2} & \text{if } \theta_m^* < \theta_0, \\ \left(\tan^2 \theta_m^* + \frac{2\delta\lambda^{\text{HWFZ}}}{\lambda_0} \right)^{1/2} - \tan \theta_m^* & \text{if } \theta_m^* > \theta_0, \end{cases} \quad (9)$$

where λ_0 is the Bragg wavelength, n_{av} is the average refractive index of a medium, and θ_0 is the threshold incident Bragg angle that defines the fulfillment of Rayleigh's criterion (see Ref. 33).

For an extended 1D measurable region, one needs a larger and thicker rejection ring, and, thus, a larger θ_m^* and a wider $\delta\theta_m^{\text{HWFZ}}$. Figure 5 shows $\delta\lambda^{\text{HWFZ}}$ in (a) and $\delta\theta_m^{\text{HWFZ}}$ in (b) of a reflecting VBG with diffraction efficiency $\eta_0 = 99.99\%$ (OD 4) and $n_{\text{av}} = 1.485$ at $\lambda_0 = 532$ nm as a function of incident Bragg angle θ_m^* for three different grating thicknesses— t_0 of 2, 5, and 10 mm. Figure 5(a) shows that within $\theta_m^* < 20^\circ$, $\delta\lambda^{\text{HWFZ}}$ is almost independent of θ_m^* , and all three cases have wide enough spectral selectivity to reject the Rayleigh scattering, having a bandwidth of 1–10 GHz (0.001–0.01 nm). According to Fig. 5(b), at $\theta_m^* < 1^\circ$, $\delta\theta_m^{\text{HWFZ}}$ monotonically increases along with θ_m^* , which is good for a larger and thicker rejection ring. However, this θ_m^* is too small to have an effective size of the rejection ring (being almost a point measurement). On the other hand, at $\theta_m^* > 1^\circ$, it is noteworthy that θ_m^* and $\delta\theta_m^{\text{HWFZ}}$ are approximately in the inversely proportional relation, being in a tradeoff. This means that one needs to control other grating parameters, e.g., one can reduce the thickness t_0 for a larger θ_m^* or $\delta\theta_m^{\text{HWFZ}}$, as shown in Fig. 5(b). Note that in this estimation, η_0 is kept the same; therefore, a thinner thickness means that a larger refractive index modulation is required. This may affect the complexity of manufacturing or the price. Nonetheless, one can pre-determine the best VBG parameters that meet specific requirements for the designed experiments.

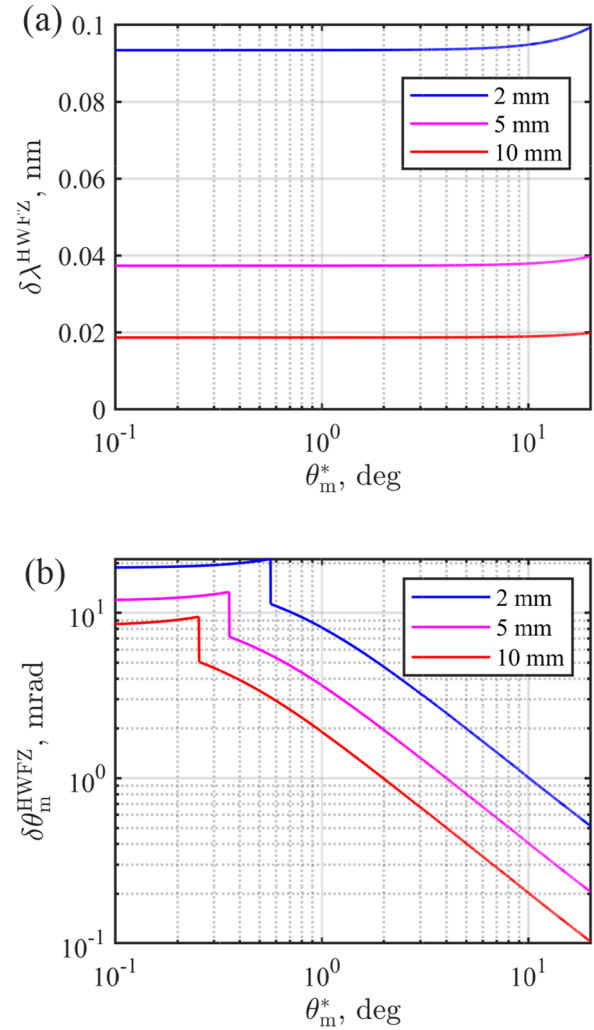


FIG. 5. (a) Spectral selectivity $\delta\lambda^{\text{HWFZ}}$ and (b) angular selectivity $\delta\theta_m^{\text{HWFZ}}$ of reflecting VBG, with 99.99% diffraction efficiency at wavelength $\lambda_0 = 532$ nm, as a function of incident Bragg angle θ_m^* at different grating thicknesses.

III. APPLICATION OF THE REJECTION RING TO 1D MEASUREMENT

A. Alignment of a VBG filter with respect to a laser line

A typical optical setup for laser light scattering diagnostics with a volume Bragg grating is shown in Fig. 6; a probing laser propagating along the x -axis (with vertical polarization in y) on the x - z plane, and light scattering collection in z direction (90° collection).

To reject the strong laser line in scattering diagnostics, a VBG is rotated. Figure 7 shows simulated laser line images, depending on a specific angle of tuning. A laser line in x direction (the white region) is simulated as a Gaussian beam focused into a beam waist of $150 \mu\text{m}$ and is given the intensity $I = 10^4$. Note that, within the viewed region, the variation of the probe beam diameter is negligible. The intensity $I = 8$ is given in the area other than the

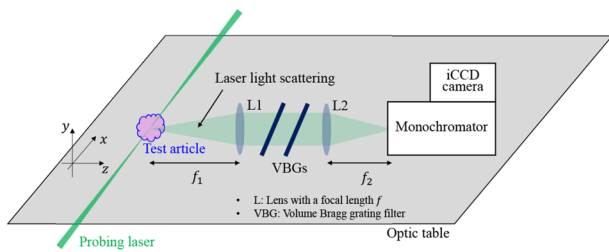


FIG. 6. Schematic of a typical optical setup for laser light scattering diagnostics with a volume Bragg grating filter.

laser image, simply to provide a little contrast on the resulting intensity map.

First, the yaw ψ tuning, Fig. 7(a), moves the rejection ring left or right (along x axis), having the rejection ring stand perpendicular to the laser. This only rejects a small portion of the laser line (given as t_r , in the shown example, $\sim 200 \mu\text{m}$), limiting the setup to a point measurement, with a resolution of t_r . On the other hand, in the totally same optical setup, by tuning the pitch ϕ , Fig. 7(b), the rejection ring moves up or down (along y axis), being tangential to the laser line. As a result, a wider spatial region (in the shown example, $\sim 2.5 \text{ mm}$) falls into the rejection ring (the high OD region), allowing a 1D spatially resolved measurement perpendicular to the laser beam propagation axis—in this case, along the y axis.

It is clear now how specific angle control can result in either a point measurement, averaged over the number of pixels blocked along the axis perpendicular to the laser beam propagation axis, or a 1D measurement, by resolving at each pixel row along this direction. Note that if a system adopts only a single angle tuning for a VBG, i.e., the yaw angle control with a rotation stage (rotation along y axis) while the probing laser is propagating along an optic table, as seen in Fig. 6, only a narrow portion of the laser is rejected, seen in Fig. 7(a). This makes a laser scattering system (one where no fiber is used) to be fundamentally limited to the point measurement. It is noteworthy that the diagnostic can be easily extended from a point measurement to a 1D measurement with the exact same experimental setup. Note that the length of $\sim 2.5 \text{ mm}$ in the example, seen in Fig. 7(b), is long enough to resolve a full radial distribution of test article properties, such as thin discharge columns, microplasmas, and streamers. More importantly, the spatial resolution perpendicular to the beam

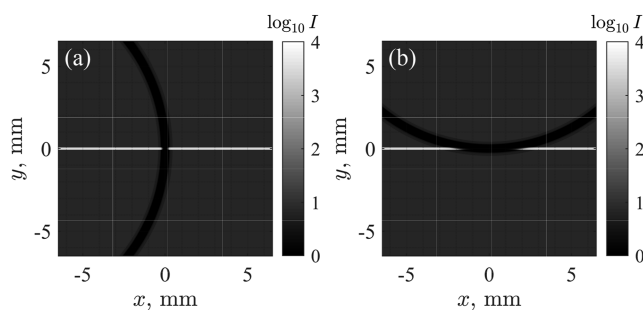


FIG. 7. Laser line rejection by tuning the VBG angle (a) $(\phi, \psi) = (0^\circ, 6^\circ)$ and (b) $(\phi, \psi) = (6^\circ, 0^\circ)$. The white line indicates a laser line image.

propagation axis, determined directly by the detector resolution and imaging optics, which can be as small as a few μm , and can also be easily adjusted by a choice of imaging optics. This is because each pixel row corresponds to a different spatial location on the object plane. Such resolution enables to resolve steep gradients.

B. Extended 1D measurement with a VBG

Considering the rejection ring size D_r or the thickness t_r being proportional to the collimation lens focal length $\propto f$, Eqs. (2)–(4), a quick method to extend the 1D measurement region is to implement a collimation lens with a longer focal length. Figure 8(a) shows such application with a different focal length ($f = 200 \text{ mm}$) of the collimation lens, where a VBG is at $(\phi, \psi) = (6^\circ, 0^\circ)$. Compared to the case of $f = 100 \text{ mm}$, seen in Fig. 7(b), the case with a collimation lens with $f = 200 \text{ mm}$, Fig. 8(a), shows that the rejection ring becomes larger (thicker), a laser line in a further wider 1D region can be rejected, extending the spatial measurement domain. However, it should be noted that, as the lens is positioned further away from the scattering volume, the solid angle for the signal collection decreases—the shown examples with $f = 100 \text{ mm}$ and $f = 200 \text{ mm}$, ~ 4 times weaker signal. Thus, there exists a tradeoff between the measurable 1D region and the total signal intensity (assuming the filter size is kept the same).

To overcome this tradeoff, one can use multiple filters, by simply adding an additional filter after one, see Fig. 6. Figure 8(b) shows laser line rejection by two VBGs—one angle tuned with $(\phi, \psi) = (6^\circ, 1^\circ)$ and another with $(\phi, \psi) = (-6^\circ, -1^\circ)$. Thus, the approximately two times extended 1D region $\sim 5.5 \text{ mm}$, can be rejected by slightly shifting the rejection rings from each filter with ψ tuning. Note that, as the total transmission of other wavelengths unaffected by the filter is typically $>90\%$, the signal loss can be significantly reduced compared to the case of using a longer focal length lens. It should be noted that this proposed method of using multiple VBGs differs from the commonly known application of multiple VBGs to improve the rejection power.

C. Demonstration of laser line rejection with a VBG notch filter

The experimental setup is similar to that shown in Fig. 6. A Nd:YAG frequency-doubled 532 nm laser (10 Hz, 5 ns; NL315-10SH, Ekspla) is used as a laser source, and images are captured by

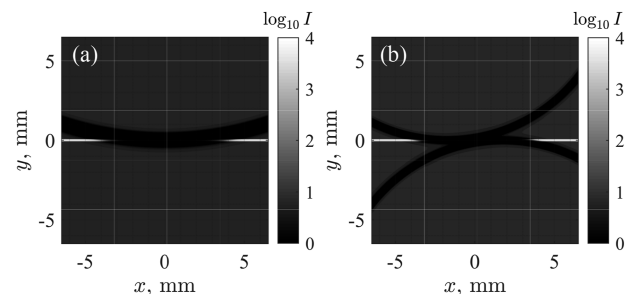


FIG. 8. Laser line rejection (a) with a collimation lens focal length $f = 200 \text{ mm}$ with $(\phi, \psi) = (6^\circ, 0^\circ)$ and (b) with two VBGs, where one is angle tuned at $(\phi, \psi) = (6^\circ, 1^\circ)$ and another with $(\phi, \psi) = (-6^\circ, -1^\circ)$.

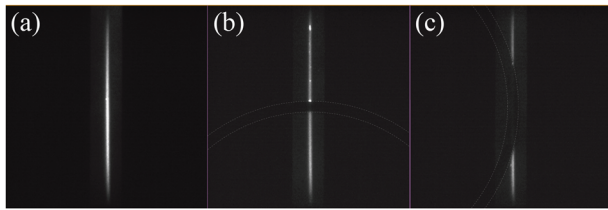


FIG. 9. Images of a laser line (a) without a VBG, (b) (ϕ, ψ) with a VBG $\approx (0^\circ, 6^\circ)$, and (c) (ϕ, ψ) with a VBG $\approx (6^\circ, 0^\circ)$. A collimation lens with a focal length $f = 100$ mm is used. The white dotted lines are added to indicate the rejection ring, for better visibility. Note that the image size is 13×13 mm² and rotated due to the rotated spectrometer and camera assembly.

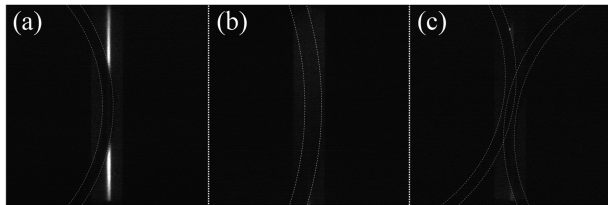


FIG. 10. Images of a laser line (a) with one VBG and a collimation lens focal length $f = 100$ mm with $(\phi, \psi) \approx (6^\circ, 0^\circ)$ and (b) with one VBG and a collimation lens focal length $f = 200$ mm with $(\phi, \psi) \approx (6^\circ, 0^\circ)$. Note the enlarged rejection ring in (b). In (c), two VBGs are used, where one is angle tuned at $(\phi, \psi) \approx (6^\circ, 1^\circ)$ and another with $(\phi, \psi) \approx (-6^\circ, -1^\circ)$. The white dotted lines are added, to indicate the rejection ring, for better visibility.

an emiCCD camera (PI-MAX4:1024EMB, Princeton Instruments). The imaging is done with 1:1 imaging optics, and the image size is 13×13 mm² for 1024×1024 pixels (the horizontal view is limited by a slit in the spectrometer). Note that the spectrometer (IsoPlane 320, Princeton Instruments) and camera assembly are rotated, to align the spectrometer slit to be parallel with the laser so that the demonstration images to be shown are 90° rotated. An OD4 VBG filter designed for 532 nm (BNF-532; OptiGrate) is used.

Figure 9 demonstrates laser line rejection (a) without a VBG, (b) with a VBG $(\phi, \psi) \approx (0^\circ, 6^\circ)$, and (c) with a VBG $(\phi, \psi) \approx (6^\circ, 0^\circ)$. Note that both—collimation lens, L1, and focusing lens, L2—have a focal length $f = 100$ mm. The white dotted curves are added, to indicate the rejection ring, for better visibility. Figures 9(b) and 9(c) correspond to the simulated cases shown in Fig. 7.

Figure 10 demonstrates laser line rejection (a) with one VBG and a collimation lens focal length $f = 100$ mm with $(\phi, \psi) \approx (6^\circ, 0^\circ)$, (b) with one VBG and a collimation lens focal length $f = 200$ mm with $(\phi, \psi) \approx (6^\circ, 0^\circ)$, and (c) with two VBGs, where one is angle tuned at $(\phi, \psi) \approx (6^\circ, 1^\circ)$ and another with $(\phi, \psi) \approx (-6^\circ, -1^\circ)$. The cases of (b) and (c) correspond to the simulated cases in Fig. 8, demonstrating the further extended spatial laser line rejection.

IV. 1D LIGHT SCATTERING DIAGNOSTICS WITH VBG FILTERS

Here, we demonstrate 1D spatially resolved light scattering measurement with VBG filters—rotational Raman scattering and Thomson scattering. A custom vacuum cell and electrode setup is

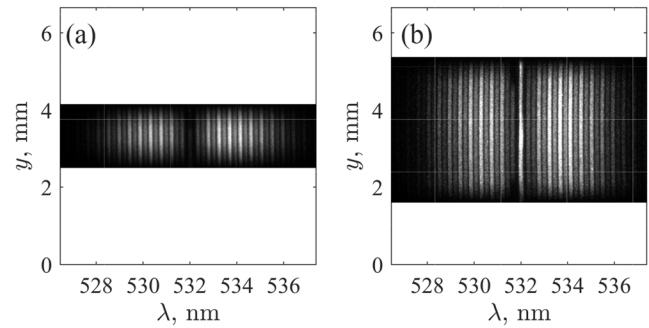


FIG. 11. Rotational Raman scattering (RRS) of nitrogen at 20 kPa (150 Torr) and room temperature, (a) with one VBG, and (b) with two VBGs. The white region is where the view is limited by an extra slit.

used to control neutral background pressure and discharge voltage conditions. Note that rotational Raman scattering on nitrogen is additionally used for absolute number density calibration of the Thomson scattered light. The general theory and data extraction methods are explained in Appendix B.

Two similar collection systems and test-beds were assembled at Georgia Tech (GT) and Texas A&M University (TAMU). For both Rotational Raman scattering (RRS) and Thomson scattering (TS) diagnostics, a 1:1 image relay is done with two $f = 200$ mm lenses, and then, the 1:2 relay into a spectrometer with a combination of a $f = 50$ mm collimation lens and a $f = 100$ mm focusing lens. At GT, a single VBG filter is placed between the collimation lens and focusing lens, while two VBG filters were placed for the experiment at TAMU. For a non-extended 1D measurement, two VBG filters are aligned so that two rejection rings overlap each other for doubled attenuation of the laser line. For an extended 1D measurement, two filters are aligned in a way as to reject an extended 1D length. At GT, a setup composed of a spectrometer (IsoPlane-320A, Princeton Instruments) and an iCCD camera (PI-MAX4:1024i, Princeton Instruments) is used, and at TAMU, the setup described in Sec. III C is used. Both systems employed Thorlabs achromatic lenses for collection, transmission, collimation, and focusing onto the spectrometers. Estimated total transmission from the used collecting optics is 76% based on the manufacturers' specification sheets. The GT experiment uses a Quantel Evergreen 532 nm Nd:YAG laser operating at 10 Hz with 135 mJ of laser energy

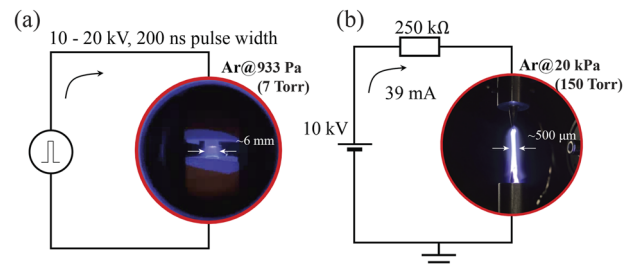


FIG. 12. Setups for plasma sources: (a) a nanosecond pulsed discharge setup and (b) a DC discharge setup.

per pulse as the interrogation beam. The TAMU experiment uses a Ekspla 532 nm Nd:YAG laser operating at 10 Hz with 175 mJ of laser energy per pulse as the interrogation beam. At GT, the nanosecond (ns) pulsed plasma discharge was driven by a nanosecond pulser (NSP-120-20F, Eagle Harbor Technologies). At TAMU, the DC plasma discharge system was driven by a steady 10-kV DC supply (EJ10P60, XP Power).

Figure 11 shows rotational Raman scattering of nitrogen at 20 kPa (150 Torr) and room temperature (a) with one VBG and (b) with two VBGs taken with the system at TAMU, where the laser

energy per pulse was 175 mJ and the camera setup was $\times 1000$ gain and 200 accumulations. The domain corresponds to the full camera pixels (1024×1024), and the white region is where the view is limited by an extra slit, to physically block the laser line not covered by the VBGs. It is notable that, with an additional VBG, the 1D measurable length is easily extended approximately two times longer than in the case with one VBG.

The same systems were used for the Thomson scattering detection. Two discharge sources are used; a nanosecond pulsed discharge with argon at 933 Pa (7 Torr) and a DC discharge with argon gas

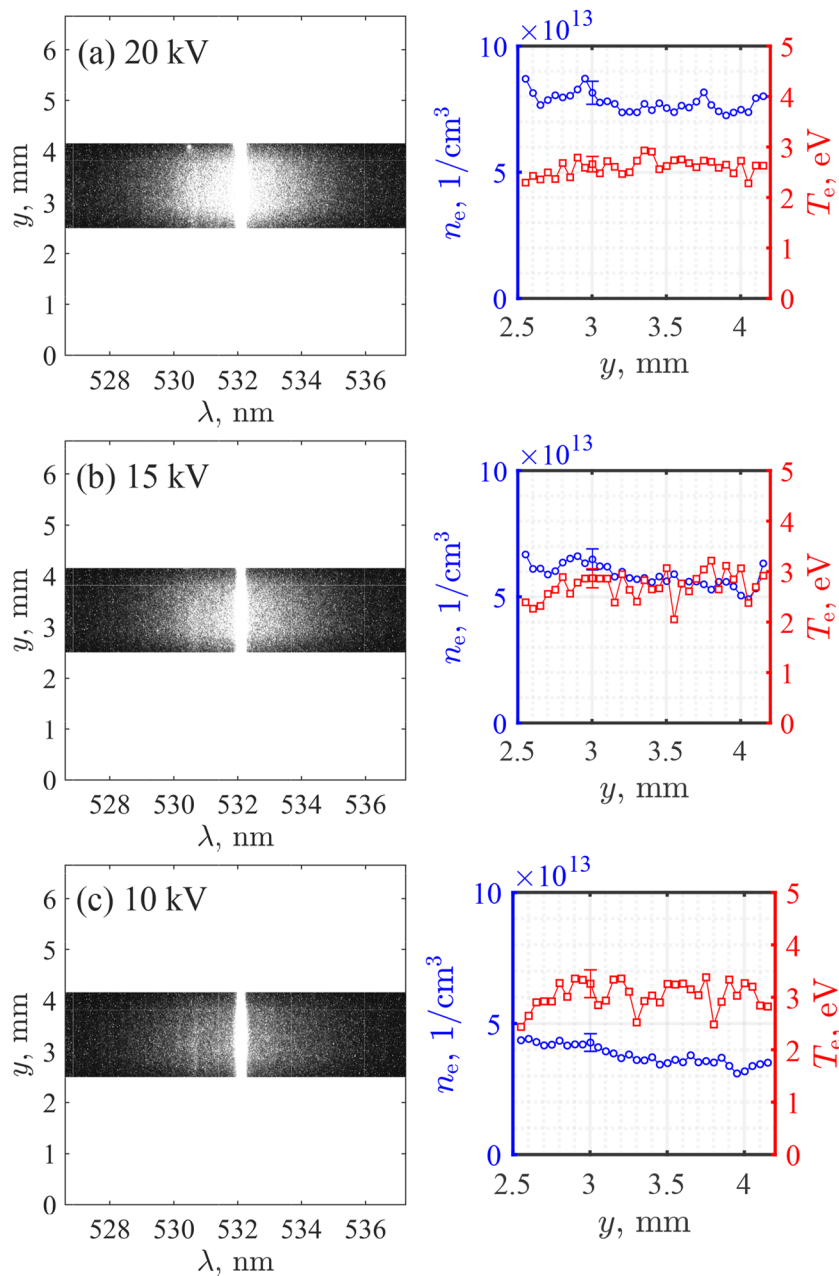


FIG. 13. Thomson scattering spectra obtained from the ns pulsed discharge. In total, three sample spectra at three different pulse voltages—(a) 20 kV, (b) 15 kV, and (c) 10 kV—are shown, and extracted spatial distributions of electron density and temperature are shown on the right hand side, where the typical 95% confidence bounds for the TS spectra fitting are shown with the error bar.

at 20 kPa (150 Torr), see Fig. 12. For TS detection, the used camera setup is $\times 100$ gain and 3000 accumulations for the nanosecond pulsed discharge case, and $\times 1000$ gain and 1000 accumulations for the steady DC discharge case.

Figure 13 shows the TS spectra from the nanosecond pulsed discharge. In total, three sample spectra at three different pulse voltages—(a) 20 kV, (b) 15 kV, and (c) 10 kV—are shown. The corresponding peak currents at the moment of the scattering collection were 32.1, 24.2, and 17.8 A. The measurement region is inside of the plasma column, the size of which is ~ 6 mm. Note that the darker region at the top and bottom of the spectra comes from various

optical aspects, such as the vignetting and varying spatial intensity of the focused laser. During the density calibration with the nitrogen RRS, the spatial distribution of the calibration coefficient is obtained, which prevents a possible artificial underestimation of plasma properties at the boundary that could come from a single calibration coefficient. A local TS spectrum is evaluated, to obtain a single point of the distribution curve at every $50\ \mu\text{m}$. Note that the spatial resolution in y direction is $6.5\ \mu\text{m}/\text{pixel}$ (1:2 imaging, and the camera resolution of $13\ \mu\text{m}/\text{pixel}$) without any pixel binning. Eventually, the TS measurement reveals the 1D distributions of electron density and temperature over the measured length within the ns discharge column.

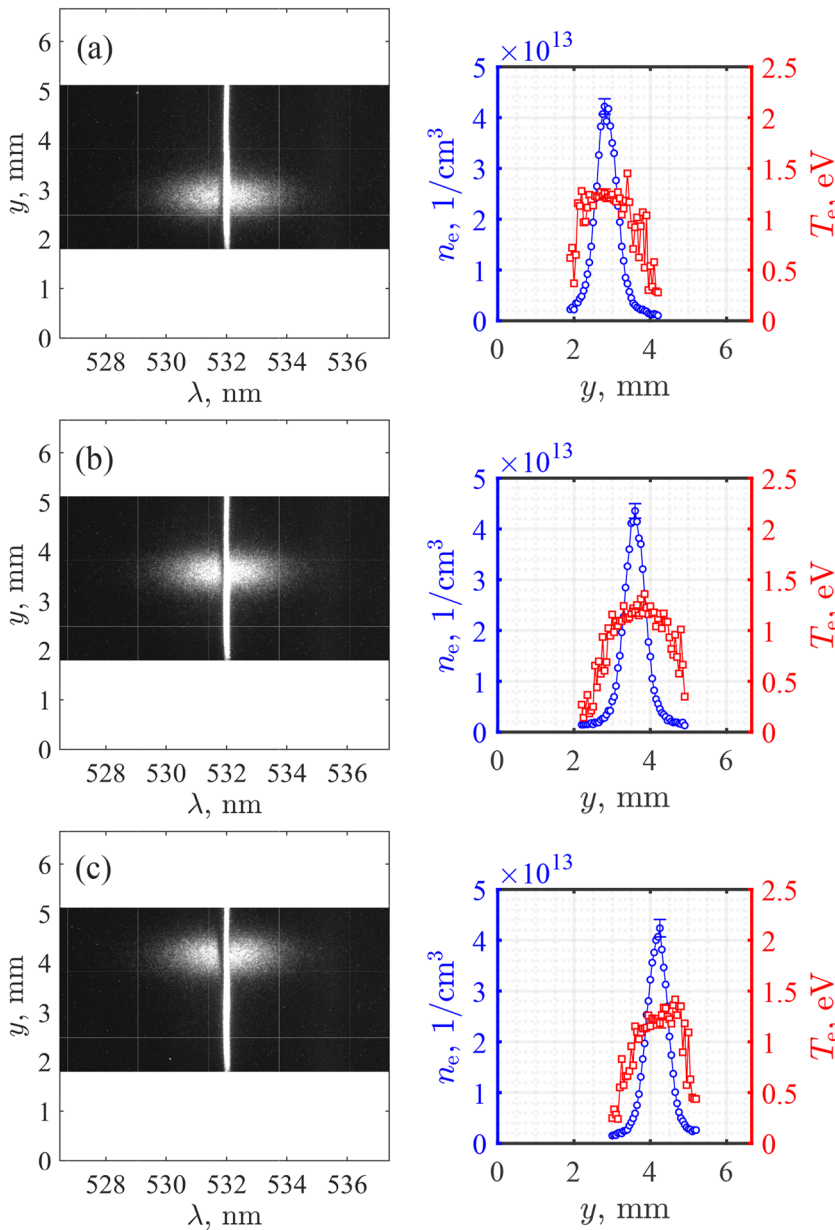


FIG. 14. Thomson scattering spectra obtained from the DC discharge. (a)–(c) show three different plasma locations within the resolving 1D region. Extracted spatial distributions of electron density and temperature are shown on the right hand side, where the typical 95% confidence bounds for the TS spectra fitting are shown with the error bar.

The coefficient of variation was evaluated to be <0.1 for the three conditions, showing a good uniformity. It should be noted that the observed uniformity could partially be from the possible plasma fluctuations and the averaging effect of the shot accumulation, rather than the instantaneous uniformity of the plasma itself. Such clarification would require further dedicated tests, which is beyond the scope of this work. Here, we confirm that the proposed method can be useful to characterize a 1D distribution.

Figure 14 shows the TS spectra from the steady DC discharge. To demonstrate the extended 1D TS measurement, the plasma column is spatially shifted while keeping the optics/optical axis fixed. Figures 14 (a)–(c) show three different plasma locations. The extracted spatial distributions of electron density and temperature are shown on the right-hand side. Again, spatial distribution of the calibration coefficient is obtained during the density calibration with the nitrogen RRS. An example of RRS used for the calibration is that shown in Fig. 11(b). Similar to the ns discharge experiment, a local TS spectrum is evaluated, to obtain a single point of the distribution curve at every $50\text{ }\mu\text{m}$. Note that the system has the same spatial resolution of $6.5\text{ }\mu\text{m}$ explained for the ns discharge. It is noteworthy that the TS is successfully captured at the extended 1D length realized by the two VBG filters. The spatial distributions of electron temperature and density confirm the identical plasma properties detected at different shifted locations. Additionally, thanks to the high resolution of the system, the sharp gradient over a few hundred μm of the plasma column is successfully captured. We note that the gradient of the instantaneous plasma could be larger.

V. CONCLUSION

We have elucidated the methodology for using a single or multiple VBG notch filters for high spatial resolution of plasma properties perpendicular to the incident interrogation beam. The systems feature compactness, simple implementation, high throughput, and flexibility, to accommodate various experimental conditions. Evaluation of the geometrical parameters of a rejection ring by a VBG based on first principles of the VBG acting as a spectral/angular filter is explained. Both simulation and experiment showed how the rejection ring position can be manipulated with a pitch/yaw tuning. It is shown that, with proper angle tuning of the VBG, a system that has traditionally been used for point measurements averaged over the small detection volume necessitated by filter alignment can be easily extended to a 1D spatially resolved measurement with the exact same setup by simply aligning the filter slightly differently. As the filter is angle sensitive, it could be less effective to reject a stray light that is not coming at a desirable angle to the filter plane. However, an additional optical technique, such as an image relay with a slit, can be implemented.

Several mathematical expressions are derived and presented, that allow for estimation of how much spatial rejection and optical attenuation of the laser line can be attainable for a given probe laser beam waist and optical collection system. For the shown example cases with a typical focused probe beam of the beam waist (or the spectrometer slit opening) $\sim 150\text{ }\mu\text{m}$, the rejection ring can provide several millimeter length for a 1D measurement.

Methods to further extend the spatial measurement region are proposed and demonstrated; using a collimation lens with a different focal length or using multiple VBG filters. The method

using multiple filters can minimize the signal loss, without the trade-off of the solid angle. Note that this proposed use of multiple VBG filters differs from the commonly known application to improve the total attenuation by extending the possible detection volume in the beam propagation axis direction.

Extended spatial measurement is greatly advantageous, as it provides further comprehensive spatial information of the test articles, such as spatial uniformity/variation of physical properties. Two different plasma sources are used, and the system successfully observed the spatial uniformity within a $\sim 6\text{ mm}$ column, or the sharp gradient over a few hundred μm with a $6.5\text{ }\mu\text{m}$ spatial resolution. It should be noted that this resolution can be easily tuned by imaging optics and pixel binning. The proposed system can be helpful to characterize plasmas that have small plasma size, of a few mm, or steep gradients.^{8,12,36–41} Note that the capability to extend 1D measurement is also highly useful to diagnose larger size test articles as well.

ACKNOWLEDGMENTS

This work was funded in part by the Office of Naval Research Grant No. N00014-20-1-2348, under Dr. Eric Marineau.

AUTHOR DECLARATIONS

Conflict of Interest

The authors have no conflicts to disclose.

Author Contributions

J. Bak: Conceptualization (lead); Data curation (equal); Formal analysis (lead); Investigation (lead); Methodology (equal); Validation (equal); Visualization (lead); Writing – original draft (lead); Writing – review & editing (equal). **J. L. Suazo Betancourt:** Data curation (equal); Formal analysis (equal); Investigation (equal); Validation (equal); Writing – original draft (supporting); Writing – review & editing (equal). **A. Rekhy:** Investigation (supporting); Methodology (equal); Writing – review & editing (equal). **A. Abbasszadehrad:** Investigation (supporting); Methodology (supporting); Writing – review & editing (equal). **R. B. Miles:** Conceptualization (supporting); Funding acquisition (lead); Project administration (lead); Resources (equal); Supervision (lead); Writing – review & editing (equal). **C. M. Limbach:** Methodology (equal); Resources (equal); Supervision (supporting); Writing – review & editing (equal). **M. L. R. Walker:** Project administration (equal); Resources (equal); Supervision (supporting); Writing – review & editing (equal).

DATA AVAILABILITY

The data that support the findings of this study are available from the corresponding author upon reasonable request.

APPENDIX A: SAMPLE SPECTRAL LINE SHAPES

Sample line spectra at specific locations are shown in Fig. 15, where (a) is the rotational Raman spectrum at $y = 3.7765\text{ mm}$

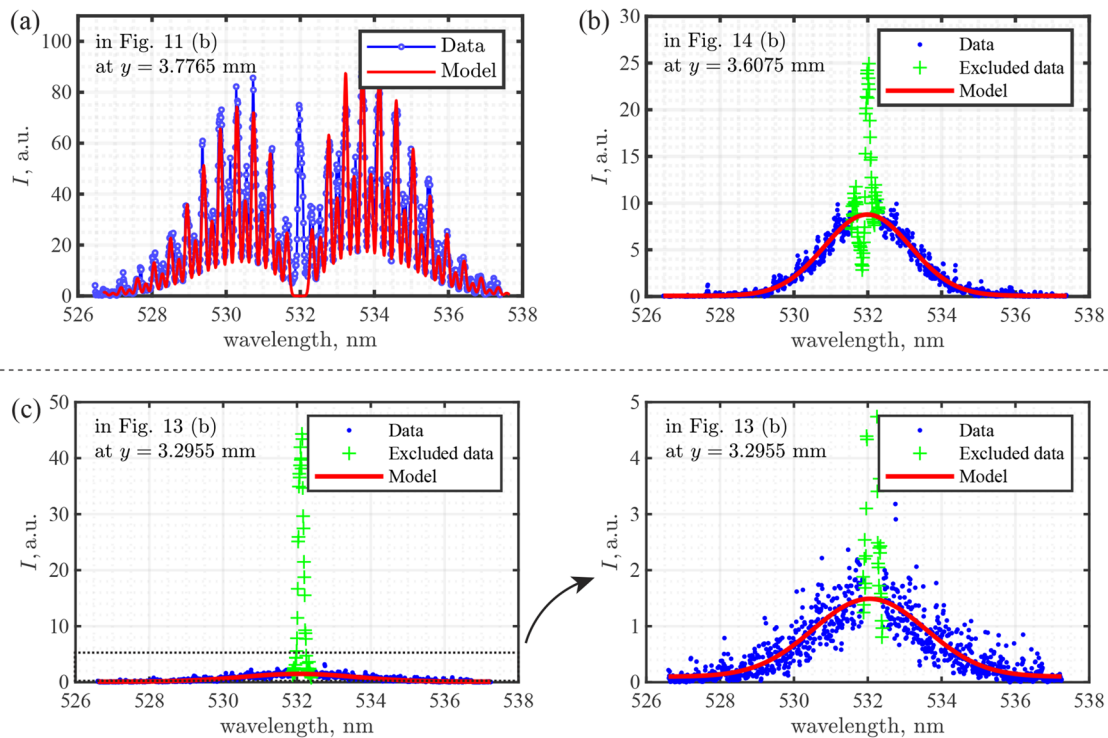


FIG. 15. Sample spectra for the figures in the manuscript are shown for comparison of the residual near-laser line lights to RRS or TS. (a) The rotational Raman spectrum at $y = 3.7765$ mm in Fig. 11(b). (b) The Thomson spectrum at $y = 3.6075$ mm in Fig. 14(b). (c) The Thomson spectrum at $y = 3.2955$ mm in Fig. 13(b), where the left figure shows the full range of the intensity, while the right figure is a zoomed-in view.

in Fig. 11(b), (b) is the Thomson spectrum at $y = 3.6075$ mm in Fig. 14(b), and (c) is the Thomson spectrum at $y = 3.2955$ mm in Fig. 13(b), where the left figure shows the full range of the intensity, while the right figure is a zoomed-in view. From (a) and (b), it is notable that the residual stray light plus the Rayleigh near the laser line (in Figs. 11 and 14) is suppressed at the same order of magnitude of the interested spectra. From (c), it can be seen that one order of magnitude stronger near-laser line is present. During the spectrum fitting, points near the laser wavelength (green cross) are excluded, as shown in the given samples.

APPENDIX B: SCATTERING OF ELECTROMAGNETIC RADIATION AND DATA ANALYSIS

Scattering of electromagnetic radiation is the process of partial re-radiation of incident electromagnetic radiation by scatterers. This process can be elastic, leading to a re-radiation at the same wavelength/frequency of the incident radiation in the frame of reference of the absorbing scatterer. This process can also be inelastic, leading to re-radiation that is at a wavelength/frequency different than that of the incident radiation in the frame of reference of the scatterer. This causes an energy transition in one of the energy modes of the scatterers undergoing the scattering process.

There are many types of electromagnetic scattering. The relevant ones in this work are Thomson scattering and rotational

Raman scattering. Thomson scattering is the elastic scattering of incident radiation from free, unbound charges. Both ions and electrons Thomson scatter, but the ion scattering cross section is several orders of magnitude smaller than that of the electron scattering cross section due to their relative masses, and, as such, very difficult to measure. In this work, we are concerned with electron Thomson scattering.

Raman scattering is the inelastic scattering of polyatomic molecules as a result of a net energy exchange between the incident radiation and the internal energy modes of the polyatomic molecule. Raman scattering can be purely rotational, purely vibrational, purely electronic, or a combination of any of the aforementioned. In this work, we are concerned with purely rotational Raman scattering, as this occurs in the frequency range closest to the incident frequency.

The quantification of the scattered power per unit of wavelength is given by⁴²

$$P_s(\lambda) = C_1 \left[(P_i L_{\text{det}} \Delta\Omega) n \frac{d\sigma}{d\Omega} \right] S(\lambda), \quad (\text{B1})$$

where the constant C_1 represents an efficiency constant, P_i , L_{det} , $\Delta\Omega$, and n being the incident laser power, detection volume length, detection solid angle, and scatterer number density, respectively. $\frac{d\sigma}{d\Omega}$ is the scattering cross section. The items in the bracket represent the total scattered power intensity. $S(\lambda)$ represents the spectral shape function, which results from the finite nature of the detection optics, light

dispersion equipment (in our case, spectrometer), and detector. This function serves to redistribute the total scattered power and follows all of the properties of a probability distribution function in the system of units chosen. Below, we present the forms of the rotational Raman and Thomson scattering equations. See Refs. 9, 11, and 26 for more details.

As long as the collection conditions remain fixed, this equation can be simplified to

$$P_s(\lambda) = Cn \frac{d\sigma}{d\Omega} S(\lambda). \quad (\text{B2})$$

1. Rotational Raman scattering

In the case of rotational Raman scattering (RRS), the equation can be specified to

$$P_s^R(\lambda) = C \sum_{J'=J\pm 2} n_J \frac{d\sigma_{J \rightarrow J'}^R}{d\Omega} S^R(\lambda - \lambda_{J \rightarrow J'}), \quad (\text{B3})$$

where n_J is the density for each state J , given as

$$n_J = \frac{n_g}{Q_R} g_J (2J+1) \exp\left[-\frac{\varepsilon_J(J)}{k_B T_g}\right]. \quad (\text{B4})$$

Note that n_g is the neutral gas number density, $Q_R = \frac{(2I+1)^2 k_B T_g}{2Bhc}$ the partition sum, $\varepsilon_J(J) = hcBJ(J+1)$ the state energy, and g_J the statistical weighting factor. For nitrogen, g_J is either 6 if J is even or 3 if J is odd. I is unity, and B is 198.973 m^{-1} . $S^R(\lambda - \lambda_{J \rightarrow J'})$ represents the shape profile, taking into account various spectrum broadening sources. In RRS, it is generally assumed that the only source of broadening is the instrument function (IF), and is modeled as a Gaussian function with a characteristic full width at half maximum (FWHM), which is related to the Gaussian standard deviation σ by $\text{FWHM} = 2\sqrt{2 \ln 2} \sigma$. We can quantify this as

$$S^R(\lambda, \sigma_{\text{IF}}) = \frac{1}{\sqrt{2\pi}\sigma_{\text{IF}}} \exp\left(-\frac{1}{2} \frac{(\lambda - \lambda_{J \rightarrow J'})^2}{\sigma_{\text{IF}}^2}\right), \quad (\text{B5})$$

which is the outcome of the convolution between the Dirac delta function $\delta(\lambda - \lambda_{J \rightarrow J'})$ and the Gaussian shape function $S(\lambda)$ and is a mathematical representation of the redistribution of the rotational Raman intensity lines due to the finite detection system.

The differential Raman cross-section $\frac{d\sigma^R}{d\Omega}$ is further broken up into its stokes and anti-stokes bands, which correspond to transitions to wavelengths above and below the incident wavelength. Each of these takes the following functional form:

$$\frac{d\sigma_{J \rightarrow J'}^R}{d\Omega} = \left[\frac{3}{4}\right] \frac{d\sigma_{\perp}^R}{d\Omega}, \quad (\text{B6})$$

where the factor $3/4$ is coming from the depolarization of RRS⁴³ and the perpendicular cross-section is given as

$$\frac{d\sigma_{\perp}^R}{d\Omega} = \left[\frac{64\pi^4}{45} \frac{\gamma^2}{\varepsilon_0^2}\right] \left[\frac{b_{J \rightarrow J'}(J)}{\lambda_{J \rightarrow J'}^4(J)}\right]. \quad (\text{B7})$$

Here, γ is the anisotropy of the molecular polarizability tensor, and the Placzek–Teller coefficient $b_{J \rightarrow J\pm 2}$ and the scattered wavelength $\lambda_{J \rightarrow J\pm 2}$ are given as

$$b_{J \rightarrow J\pm 2}(J) = \frac{3(2J+1\pm 1)(2J+1\pm 3)}{4(2J+1)(2J+1\pm 2)} \quad (\text{B8})$$

and

$$\lambda_{J \rightarrow J\pm 2}(J) = \lambda_i \pm \lambda_i^2 \frac{B}{hc} (4J+2\pm 4), \quad (\text{B9})$$

respectively. The “ \pm ” sign corresponds to the stokes and anti-stokes portions of the spectrum, respectively.

Given a rotational Raman spectrum collected at a given number of accumulations, detector gate, and laser energy, at a known pressure and temperature, a fitting procedure can be used to determine C and σ_{IF} as a function of spatial location. Collecting the Thomson spectra at the same collection conditions allows for C to be used as the calibration constant for the absolute number density.

2. Thomson scattering

In the case of Thomson scattering (TS),

$$P_s^T(\lambda) = C \left[n_e \frac{d\sigma^T}{d\Omega} \right] S^T(\lambda), \quad (\text{B10})$$

with the cross section being equal to the classical electron radius as

$$\frac{d\sigma^T}{d\Omega} = r_e^2 \equiv \frac{e^2}{4\pi\varepsilon_0 m_e c^2}. \quad (\text{B11})$$

Assuming a Maxwellian velocity distribution and neglecting the instrument broadening on the Thomson spectrum, as is typically done, the redistribution operation is a simple multiplication given by the following:

$$S^T(\lambda) = \frac{d\omega}{d\lambda} S^T(\omega), \quad (\text{B12})$$

where

$$S^T(\omega) = \sqrt{\frac{m_e}{2\pi k_B T_e k^2}} \exp\left(\frac{1}{2} \frac{(\omega_i - \omega_s - k v_d)^2}{2k_B T_e k^2} \right) / m_e, \quad (\text{B13})$$

with

$$\omega = \frac{2\pi c}{n} \frac{1}{\lambda}, \quad (\text{B14})$$

$$\frac{d\omega}{d\lambda} = \frac{2\pi c}{n} \frac{1}{\lambda^2}, \quad (\text{B15})$$

$$k^2 = k_s^2 + k_i^2 - 2k_i k_s, \quad (\text{B16})$$

$$k = \frac{2\pi}{\lambda}. \quad (\text{B17})$$

The $d\omega/d\lambda$ is necessary to preserve the probability density function integral being unity when being cast in the wavelength domain. With C from the Raman calibration, this can easily be fit to determine n_e and T_e for a given Thomson spectrum collected with the same collection conditions.

3. Use of rotational Raman scattering for absolute intensity calibration in applications involving light filtering

For absolute intensity calibration of Thomson scattering, Rayleigh scattering or rotational Raman scattering is commonly considered, since the intensity of such scatterings can be calculated from the absolute cross-sections and known physical properties of a gas sample.⁹ When applications involve light filtering, as in the present work, one should pay attention as to whether the filtering is done on the scattering being used for the calibration. Generally, the filtering involves the central narrowband lights, which affect the Rayleigh scattering; the Raman calibration becomes much simpler and more proper over the Rayleigh calibration as the Raman peaks are unaffected by the filtering. Rotational Raman overlaps the Thomson scattering spectrum, so, no spectral corrections need to be made.

For instance, let us consider the Rayleigh calibration in the present application using a VBG having the rejection bandwidth of 5 cm^{-1} . Assuming that the stray light is independent of gas pressure and is constant in the setup, one may obtain a pure stray light intensity at a high vacuum, where Rayleigh becomes negligible. Subtracting it from the central intensity, which consists of Rayleigh scattering and stray light, one may obtain pure Rayleigh intensity as a function of pressure, which may be used for density calibration. However, the Rayleigh has a linewidth of order of 1–10 GHz, which totally falls within the filter's bandwidth ($5\text{ cm}^{-1} = 150\text{ GHz}$). Since the Rayleigh scattering is filtered to some extent, it requires an additional process, to find such an attenuation factor. These issues can be avoided by using rotational Raman for calibration. The first rotational Raman line of nitrogen falls 360 GHz from the laser and well outside the VBG filter.

Rayleigh calibration may be more proper for high temperature/high-density plasma or high vacuum applications where Thomson scattering is dominant. For such a case, there is no need for a filter to collect the total unfiltered Rayleigh signal, but gas pressure in the test vessel may need to be elevated, to obtain a Rayleigh signal comparable with TS.⁷

REFERENCES

- ¹M. N. Shneider, "Ponderomotive perturbations of low density low-temperature plasma under laser Thomson scattering diagnostics," *Phys. Plasmas* **24**, 100701 (2017).
- ²E. A. D. Carbone, J. M. Palomares, S. Hübner, E. Iordanova, and J. J. A. M. van der Mullen, "Revision of the criterion to avoid electron heating during laser aided plasma diagnostics (LAPD)," *J. Instrum.* **7**, C01016 (2012).
- ³R. B. Miles, W. R. Lempert, and J. N. Forkey, "Laser Rayleigh scattering," *Meas. Sci. Technol.* **12**, R33 (2001).
- ⁴B. Vincent, S. Tsikata, and S. Mazouffre, "Incoherent Thomson scattering measurements of electron properties in a conventional and magnetically-shielded Hall thruster," *Plasma Sources Sci. Technol.* **29**, 035015 (2020).
- ⁵D. L. Crintea, D. Luggenhölscher, V. A. Kadetov, C. Isenberg, and U. Czarnetzki, "Phase resolved measurement of anisotropic electron velocity distribution functions in a radio-frequency discharge," *J. Phys. D: Appl. Phys.* **41**, 082003 (2008).
- ⁶A. L. Milder, S. T. Ivancic, J. P. Palastro, and D. H. Froula, "Impact of non-Maxwellian electron velocity distribution functions on inferred plasma parameters in collective Thomson scattering," *Phys. Plasmas* **26**, 022711 (2019).
- ⁷J. Sheffield, D. Froula, S. H. Glenzer, and N. C. J. Luhmann, *Plasma Scattering of Electromagnetic Radiation* (Elsevier, 2011).
- ⁸S. Hübner, J. S. Sousa, J. van der Mullen, and W. G. Graham, "Thomson scattering on non-thermal atmospheric pressure plasma jets," *Plasma Sources Sci. Technol.* **24**, 054005 (2017).
- ⁹M. v. d. Sande, "Laser scattering on low temperature plasmas: High resolution and stray light rejection," Ph.D. thesis, Technische Universiteit Eindhoven, 2002.
- ¹⁰K. Tomita, S. Yoshitake, K. Uchino, D. Takenaka, H. Toda, M. Hikita, and K. Suzuki, "Measurements of electron density and electron temperature of arc discharge plasmas containing metallic vapors using laser Thomson scattering," *Electr. Eng. Jpn* **188**, 1–8 (2014).
- ¹¹E. Carbone and S. Nijdam, "Thomson scattering on non-equilibrium low density plasmas: Principles, practice and challenges," *Plasma Phys. Controlled Fusion* **57**, 014026 (2015).
- ¹²K. Sasaki, S. Soma, H. Akashi, M. Elabbagh, and Y. Ikeda, "Electron temperatures and electron densities in microwave helium discharges with pressures higher than 0.1 MPa," *Contrib. Plasma Phys.* **55**, 563–569 (2015).
- ¹³A. Roettgen, I. Shkurenkov, M. Simeni Simeni, V. Petrishchev, I. V. Adamovich, and W. R. Lempert, "Time-resolved electron density and electron temperature measurements in nanosecond pulse discharges in helium," *Plasma Sources Sci. Technol.* **25**, 055009 (2016).
- ¹⁴A. Obrusník, P. Synek, S. Hübner, J. J. A. M. van der Mullen, L. Zajíčková, and S. Nijdam, "Coherent and incoherent Thomson scattering on an argon/hydrogen microwave plasma torch with transient behaviour," *Plasma Sources Sci. Technol.* **25**, 055018 (2016).
- ¹⁵K. Tomita, Y. Inada, A. Komuro, X. Zhang, K. Uchino, and R. Ono, "Measurement of electron velocity distribution function in a pulsed positive streamer discharge in atmospheric-pressure air," *J. Phys. D: Appl. Phys.* **53**, 08LT01 (2020).
- ¹⁶W.-q. Tan, Y.-y. Liu, X.-y. Li, P. Yuan, H. Zhao, Z.-c. Li, and J. Zheng, "Electron density measurement via dual-angle Thomson scattering diagnosis," *J. Appl. Phys.* **129**, 043302 (2021).
- ¹⁷L. P. Bakker and G. M. W. Kroesen, "Thomson scattering in a low-pressure neon mercury positive column," *J. Appl. Phys.* **90**, 3720–3725 (2001).
- ¹⁸W. Lee and W. R. Lempert, "Spectrally filtered Raman/Thomson scattering using a rubidium vapor filter," *AIAA J.* **40**, 2504–2510 (2002).
- ¹⁹C. M. Limbach and R. B. Miles, "Rayleigh and Thomson scattering diagnostics of laser air sparks: A testbed for tailoring laser plasmas," 45th AIAA Plasmadynamics and Lasers Conference, 2014.
- ²⁰H. J. Weßeling and B. Kronast, "Discrepancies between Thomson-light-scattering results and those obtained from E/N measurements in a helium glow discharge," *Europhys. Lett.* **33**, 273–278 (1996).
- ²¹T. Y. Chen, A. C. Rouso, S. Wu, B. M. Goldberg, H. Van Der Meiden, Y. Ju, and E. Kolemen, "Time-resolved characterization of plasma properties in a CH₄/He nanosecond-pulsed dielectric barrier discharge," *J. Phys. D: Appl. Phys.* **52**, 18LT02 (2019).
- ²²F. Wu, J. Li, Y. Xian, X. Tan, and X. Lu, "Investigation on the electron density and temperature in a nanosecond pulsed helium plasma jet with Thomson scattering," *Plasma Processes Polym.* **18**, 2100033 (2021).
- ²³M. Paillet, F. Meunier, M. Verhaegen, S. Blais-Ouellette, and R. Martel, "High performance resonance Raman spectroscopy using volume Bragg gratings as tunable light filters," *Rev. Sci. Instrum.* **81**, 053111 (2010).
- ²⁴A. L. Glebov, O. Mokhun, A. Rapaport, S. Vergnole, V. Smirnov, and L. B. Glebov, "Volume Bragg gratings as ultra-narrow and multiband optical filters," in *Micro-Optics*, edited by H. Thienpont, J. Mohr, H. Zappe, and H. Nakajima (SPIE, 2012), Vol. 8428, p. 84280C10.1117/12.923575.
- ²⁵B. L. M. Klarenaar, F. Brehmer, S. Welzel, H. J. van der Meiden, M. C. M. van de Sanden, and R. Engeln, "Note: Rotational Raman scattering on CO₂ plasma using a volume Bragg grating as a notch filter," *Rev. Sci. Instrum.* **86**, 046106 (2015).
- ²⁶B. Vincent, S. Tsikata, S. Mazouffre, T. Minea, and J. Fils, "A compact new incoherent Thomson scattering diagnostic for low-temperature plasma studies," *Plasma Sources Sci. Technol.* **27**, 055002 (2018).
- ²⁷Y. Wu, C. Limbach, and R. B. Miles, "Spatially and temporally resolved electron temperature and number density measurements in 100-kHz nanosecond pulse burst discharges using Laser Thomson scattering," in *AIAA Scitech 2021 Forum* (American Institute of Aeronautics and Astronautics, Reston, VA, 2021), pp. 1–9.

- ²⁸E. Slikboer and J. Walsh, "Impact of electrical grounding conditions on plasma-liquid interactions using Thomson scattering on a pulsed argon jet," *Sci. Rep.* **11**, 17749 (2021).
- ²⁹S. Yatom, T. Oldham, and E. Thimsen, "Characterization of plasma in RF jet interacting with water: Thomson scattering versus spectral line broadening," *Plasma Sources Sci. Technol.* **31**, 035018 (2022).
- ³⁰B. L. M. Klarenaar, O. Guaitella, R. Engeln, and A. Sobota, "How dielectric, metallic and liquid targets influence the evolution of electron properties in a pulsed He jet measured by Thomson and Raman scattering," *Plasma Sources Sci. Technol.* **27**, 085004 (2018).
- ³¹I. V. Ciapurin, L. B. Glebov, and V. I. Smirnov, "Modeling of Gaussian beam diffraction on volume Bragg gratings in PTR glass," in *Practical Holography XIX: Materials and Applications* (SPIE, 2005), Vol. 5742, p. 183.
- ³²I. V. Ciapurin, L. B. Glebov, and V. I. Smirnov, "Modeling of phase volume diffractive gratings, part 1: transmitting sinusoidal uniform gratings," *Opt. Eng.* **45**, 015802 (2006).
- ³³I. V. Ciapurin, D. R. Drachenberg, V. I. Smirnov, G. B. Venus, and L. B. Glebov, "Modeling of phase volume diffractive gratings, part 2: Reflecting sinusoidal uniform gratings, Bragg mirrors," *Opt. Eng.* **51**, 058001 (2012).
- ³⁴S. C. Barden, J. A. Arns, and W. S. Colburn, "Volume-phase holographic gratings and their potential for astronomical applications," in *Optical Astronomical Instrumentation*, edited by S. D'Odorico (SPIE, 1998), Vol. 3355, pp. 866–876.
- ³⁵H. Kogelnik, "Coupled wave theory for thick hologram gratings," *Bell Syst. Tech. J.* **48**, 2909–2947 (1969).
- ³⁶N. Y. Babaeva and G. V. Naidis, "Universal nature and specific features of streamers in various dielectric media," *J. Phys. D: Appl. Phys.* **54**, 223002 (2021).
- ³⁷M. J. Johnson, D. R. Boris, T. B. Petrova, and S. G. Walton, "Spatio-temporal characterization of a pulsed DC atmospheric pressure plasma jet interacting with substrates," *J. Phys. D: Appl. Phys.* **54**, 085202 (2020).
- ³⁸A. Alberti, A. Munafò, C. Pantano, J. B. Freund, and M. Panesi, "Collinear dual-pulse laser optical breakdown and energy deposition," *J. Phys. D: Appl. Phys.* **53**, 205202 (2020).
- ³⁹T. Darny, G. Bauville, M. Fleury, S. Pasquiers, and J. Santos Sousa, "Periodic forced flow in a nanosecond pulsed cold atmospheric pressure argon plasma jet," *Plasma Sources Sci. Technol.* **30**, 105021 (2021).
- ⁴⁰P. Viegas, E. Slikboer, Z. Bonaventura, O. Guaitella, A. Sobota, and A. Bourdon, "Physics of plasma jets and interaction with surfaces: Review on modelling and experiments," *Plasma Sources Sci. Technol.* **31**, 053001 (2022).
- ⁴¹A. P. Singh, U. P. Padhi, and R. Joarder, "Insight into the evolution of laser-induced plasma during successive deposition of laser energy," *J. Appl. Phys.* **131**, 073301 (2022).
- ⁴²A. F. H. Van Gessel, E. A. D. Carbone, P. J. Bruggeman, and J. J. A. M. Van Der Mullen, "Laser scattering on an atmospheric pressure plasma jet: Disentangling Rayleigh, Raman and Thomson scattering," *Plasma Sources Sci. Technol.* **21**, 015003 (2012).
- ⁴³C. M. Penney, R. L. St. Peters, and M. Lapp, "Absolute rotational Raman cross sections for N₂, O₂, and CO₂," *J. Opt. Soc. Am.* **64**, 712 (1974).